Hindawi
Mathematical Problems in Engineering
Volume 2023, Article ID 9798267, 1 page
https://doi.org/10.1155/2023/9798267

Retraction

Retracted: Application of Multi-Measurement Vector Based on the Wireless Sensor Network in Mechanical Fault Diagnosis

Mathematical Problems in Engineering

Received 26 September 2023; Accepted 26 September 2023; Published 27 September 2023

This article has been retracted by Hindawi following an investigation undertaken by the publisher [1]. This investigation has uncovered evidence of one or more of the following indicators of systematic manipulation of the publication process:

(1) Discrepancies in scope
(2) Discrepancies in the description of the research reported
(3) Discrepancies between the availability of data and the research described
(4) Inappropriate citations
(5) Incoherent, meaningless and/or irrelevant content included in the article
(6) Peer-review manipulation

The presence of these indicators undermines our confidence in the integrity of the article's content and we cannot, therefore, vouch for its reliability. Please note that this notice is intended solely to alert readers that the content of this article is unreliable. We have not investigated whether authors were aware of or involved in the systematic manipulation of the publication process.

Wiley and Hindawi regrets that the usual quality checks did not identify these issues before publication and have since put additional measures in place to safeguard research integrity.

We wish to credit our own Research Integrity and Research Publishing teams and anonymous and named external researchers and research integrity experts for contributing to this investigation.

The corresponding author, as the representative of all authors, has been given the opportunity to register their agreement or disagreement to this retraction. We have kept a record of any response received.

References

[1] W. Kang, "Application of Multi-Measurement Vector Based on the Wireless Sensor Network in Mechanical Fault Diagnosis," *Mathematical Problems in Engineering*, vol. 2022, Article ID 2390119, 7 pages, 2022.

Hindawi
Mathematical Problems in Engineering
Volume 2022, Article ID 2390119, 7 pages
https://doi.org/10.1155/2022/2390119

Research Article

Application of Multi-Measurement Vector Based on the Wireless Sensor Network in Mechanical Fault Diagnosis

Wei Kang

Anshan Normal University Liaoning China, Anshan 114007, Liaoning, China

Correspondence should be addressed to Wei Kang; 1117410434@st.usst.edu.cn

Received 26 June 2022; Accepted 20 August 2022; Published 7 September 2022

Academic Editor: Hengchang Jing

In order to solve the problem of low positioning accuracy of mechanical fault diagnosis, a polarization GPR imaging reconstruction algorithm based on the MMV model was proposed. The algorithm was mainly based on the joint processing of the measured data of multiple polarization channels to achieve the reconstruction of the reflectance of the detection scene corresponding to each polarization channel. The simulation data processing results based on FDTD showed that compared with the traditional SMV model polarization imaging algorithm, the proposed imaging algorithm could improve the accuracy of target location reconstruction and the ability of background clutter suppression significantly. Compared with the SMV model, TCR obtained by the MMV model increased by 30%. As for the imaging results at different noise ratios, TCR obtained by the MMV model was 10% higher than that obtained by the SMV model. And when the ratio of available real data samples decreased to 25%, the sample data generation based on the adversarial generation network could greatly improve the classification accuracy of the fault diagnosis model. It could realize the detection of the target better, so as to locate faults accurately.

1. Introduction

In the increasingly intelligent society, the application of mechanical equipment is more and more widely in industrial production and daily life. From aerospace, industrial production, and national defense to the travel means of transportation, such as aircraft, cars, and high-speed train which are closely related to people's lives, rotating machinery plays an important role. With the continuous development of modern science and technology, all kinds of mechanical systems are developing towards the large-scale, complex, and high-speed direction, which also increases the uncertainty of mechanical system safety. Once the rotating machinery equipment breaks down, it will not only cause the stagnation of industrial production but also cause serious safety problems. In addition to affecting the production efficiency and economic loss of the enterprise, it may also bring irreversible casualties [1]. Mechanical equipment fault diagnosis is a scientific technology to monitor, diagnose, and predict the state of continuous running equipment and ensure the safe operation of mechanical equipment. Its outstanding characteristic is the close combination of theoretical research and engineering practical application. It is a kind of advanced technology that uses various measurement and monitoring methods to record and analyze the equipment state and identify and alarm the abnormal state (see Figure 1). Using this technology, the failure state of mechanical equipment can be found in time to avoid the occurrence of catastrophic events. It can also avoid the economic loss caused by insufficient or excessive maintenance and has greater economic benefits. As the most important part of the mechanical system, rotating machinery, such as induction motor, is the main device to drive all kinds of mechanical equipment, widely used in all kinds of mechanical equipment. The reliability and security of its operation should be higher. Generally, mechanical equipment is divided into three basic parts, gear, bearing, and rotating shafting. While rotating parts, such as bearings and gears, are also widely used in all kinds of mechanical systems. According to the survey, bearing damage and gear failure account for about 40% of the faults of rotating machinery, and 10.3% of the faults caused by gear failure [2]. Therefore,

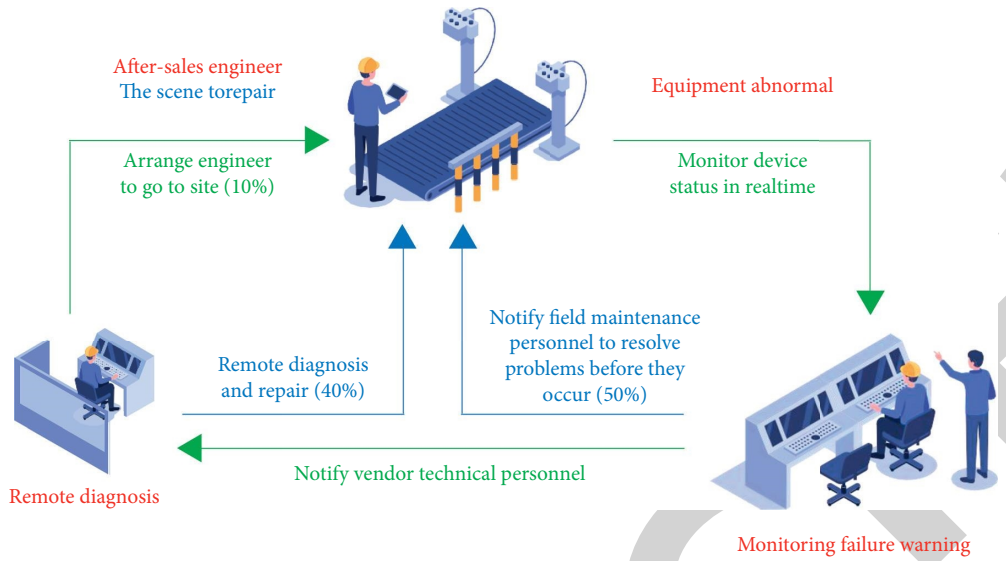

Figure 1: Mechanical fault diagnosis.

it is of great significance to find out the fault status of the rotating machinery in time and to make accurate fault diagnosis and maintenance for the rotating machinery so as to ensure the safe and stable operation of the production system and reduce the probability of catastrophic accidents.

2. Literature Review

With the development of network technology, multi-measurement vector machine fault diagnosis technology has been paid more attention. In the aspect of signal processing and feature extraction, vibration signals of rotating machinery parts are complicated when faults occur, and the signals obtained by sensors are nonlinear, non-stationary, and noisy. Therefore, it is difficult to extract useful fault features directly from original signals. Feature extraction based on signal processing is widely used in fault diagnosis. The traditional signal processing technology mainly consists of three aspects: time-domain analysis, frequency domain analysis, and time-frequency domain analysis. Time domain processing is mainly based on statistical feature analysis. The frequency domain processing method mainly analyzes the signal frequency domain components. Fourier transform is the classical frequency domain processing method, in addition to envelope analysis, thinning spectrum, cepstrum, high order spectrum, holographic spectrum analysis, and other methods. A more widely used method is the time-frequency domain analysis method, which can capture the fault-related transient components in non-stationary signals and provide the joint distribution of time domain and frequency domain, such as short-time Fourier transform, Winger-Ville distribution, empirical mode decomposition, and wavelet transform theory. Gonzalez–Arango et al. proposed the deep learning model, which got rid of the inevitable uncertainty of artificial feature extraction and enhanced the structural depth of the network model [3]. Hriez et al. proposed a software measurement method to scientifically organize the whole process of software and also proposed a method that can be used for many times in this process [4]. Shahid et al. proposed the rationality of assumptions required by the MMV model combined with sparse reconstruction, that is, when multiple observation signals share a sparse structure, the MMV model is superior to the SMV model [5]. Qi et al. proposed a feature extraction method for mechanical faults based on category-independent component analysis and the correlation coefficient. Firstly, the independent component analysis of mechanical fault signals in different working conditions were carried out to obtain the independent components of various working conditions, which contained some inherent characteristics of the working conditions. Then, the absolute sum of the correlation coefficients between the sample and the independent components extracted from signals under different working conditions was used as the characteristics of the sample [6]. Sharma et al. used the Morlet wavelet and the particle swarm optimization algorithm to de-noise bearing vibration signals [7]. Kim et al. proposed empirical mode decomposition based on adaptive variable-scale frequency-shift band-pass stochastic resonance denoising, a denoising method of a vibration signal with an interval threshold of empirical mode decomposition [8]. Gong et al. proposed a rolling bearing fault feature extraction method based on the improved envelope spectrum based on EMD and spectrum kurtosis, namely, the holographic spectrum technique for mechanical fault diagnosis [9]. Shriram et al. proposed the method of the multi-scale envelope order spectrum to evaluate the health status of the mechanical system under variable speed conditions and used the instantaneous frequency obtained by the empirical mode decomposition method to detect the state degradation of bearings [10]. Ma et al. used wavelet packet decomposition to decompose the original signal into a series of time-domain waveforms and reduced them into one-dimensional signals by local tangent space arrangement, so as to achieve denoising of the original

signal [11]. Bashar et al. combined continuous wavelet transform and local tangent space arrangement for nonlinear noise reduction [12]. Based on the characteristics of mixed time-frequency domain, Ping et al. carried out fault diagnosis of the wind turbine transmission system [13]. Chen et al. introduced an iterative algorithm for matching demodulation transformation to generate time-frequency distribution images of energy concentration. It was beneficial to weak fault feature extraction. Good results were achieved in the simulation signal and real data [14].

To solve the above problems, a sparse imaging reconstruction algorithm of polarization GPR based on the MMV model for mechanical diagnostic echo signals was proposed, which equivalently transformed the measured data of each polarization channel into multiple measurement vectors. The multi-task Bayesian compressed sensing (MT-BCS) algorithm was used to process the measurement data of different polarization channels, and then the sparse high-resolution imaging reconstruction of the mechanical fault detection region was realized. Compared with the traditional SMV reconstruction algorithm, the proposed algorithm could reduce the background clutter and improve the quality of image reconstruction, so as to achieve the accurate judgment of mechanical failure.

3. Research Methods

3.1. Traditional SRC Model. If multi-measurement vectors can share the sparse structure, the prior information can be used to constrain the selection of representation atoms to improve the performance of joint sparse reconstruction. However, in practical application, it is difficult to obtain measurement vectors with exactly the same sparse structure. Few signal sources meet the assumption conditions of the shared sparse structure. And these measurement vectors may not share the sparse structure even if they observe the same thing. The possible reasons are as follows: first, the sparsity structure of actual signals is time-varying. Second, the high dimension of the signal makes the feature space of the same type of the signal may have a large gap. For example, the photos taken by the same person under different circumstances may have a large gap. Third, the limitation of feature description space makes the measurement matrix lack feature description atoms, resulting in incomplete feature description. It can be seen that measurement vectors with identical sparse structures are difficult to obtain. In the MMV model, the general sparsity hypothesis is only valid for a small number of measurement vectors. In practical application, multi-measurement vectors with the non-shared sparse structure are often encountered [15]. The measurement vector of the traditional SRC model is single. However, intuitively, the information provided by multiple observation signals obtained from the same object is significantly more than that provided by a single observation signal. Even if these multiple observation signals do not share the sparse structure, they should still provide more effective information. If the increased information can be effectively utilized, the performance of sparse classification can be improved. In the data dictionary of the SRC model, similar training sample sets are arranged. If multiple measurement vectors are observations of the same object, then their representation atoms should be concentrated in a certain region of the measurement matrix. The corresponding representation coefficient is non-0, but the non-0 elements are not necessarily in the same line, that is, the sparse structure is not shared [16]. The non-zero terms of the coefficient matrix are concentrated in a certain category, but the sparse structure is not shared among the columns of the coefficient matrix. This prior structural information can be used to improve the accuracy of diagnosis [17].

3.2. Polarization Signal Model. The schematic diagram of polarization GPR system detection is shown in Figure 2. The polarization GPR antenna system has four polarization measurement channels, which are *XX, XY, YX,* and *YY* polarization, among which the first represents the polarization direction of the transmitting antenna and the second represents the polarization direction of the receiving antenna. The direction of the measuring line is parallel to the Y direction. Assuming that the system adopts the working mode of single station stepping frequency, for the lth $(l = 1, 2, 3, 4)$ polarization channel, the system at the mth $(m = 0, 1, \ldots, M-1)$ antenna positions and the nth $(n = 0, 1, \ldots, N-1)$ measurement data $r_l(m, n)$ of frequency points are expressed as the following formula:

$$r_l(m,n) = \sum_{p=1}^{p} \delta_{p,l} \exp\left(-j2\pi f_n \tau_{p,m}\right). \tag{1}$$

In the formula, $\delta_{p,l}$ is the complex reflection coefficient of the pth target. $f_n = f_0 + n\Delta f$ is the nth working frequency point. f_0 is the starting frequency of the working bandwidth. Δf is the step interval of frequency in the working bandwidth. $\tau_{p,m}$ is the round-trip delay between the pth target and the mth antenna position.

The detection area is divided into $N_y \times N_z$ uniform spatial grids, where N_y and N_z represent the number of discrete grids in horizontal direction and depth direction, respectively. The reconstructed image can be transformed into $N_y N_z \times 1$-dimensional scene reflectance vector δ_l by column stacking operation. Then the received signal r_l of the system in the lth polarization channel can be expressed as the following formula:

$$r_l = \psi \delta_l. \tag{2}$$

In the formula, $r_l = [r_l(0,0), \ldots, r_l(0, N-1), r_l(M-1, N-1)]^T$. δ_l represents the scene reflectance vector corresponding to the lth polarization measurement channel. ψ is the $MN \times N_y N_z$-dimensional lexicographical matrix, and the elements in the rth row and qth column can be expressed as the following formula:

$$[\psi]_{r,q} = \exp\left(-j2\pi f_n \tau_{p,m}\right). \tag{3}$$

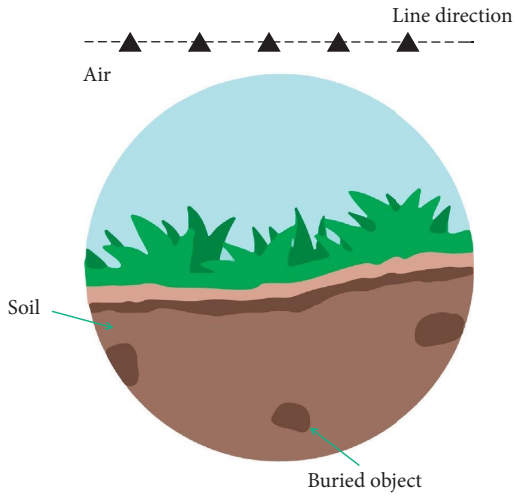

Figure 2: Schematic diagram of system detection.

In the formula, $r = 0, 1, MN - 1$; $q = 0, 1, N_y N_z - 1$; $n = r \bmod N$; $m = [r/N]$. $\tau_{p,m}$ represents the round-trip delay between q imaging grid and m_{th} antenna location.

Because the target of interest only occupies a few space positions in the detection scene, δ_l is a sparse vector. A random measurement matrix ϕ_l can be constructed to achieve the reduction sampling and obtain the measurement vector, as shown in the following formula:

$$y_l = \phi_l r_l = \phi_l \psi \delta_l = A_l \delta_l + n_l. \tag{4}$$

In the formula, $A_l = \phi_l \psi$ is a $J \times MN$ dimensional matrix, which can be constructed by randomly selecting J rows from the $MN \times MN$ dimensional identity matrix. The dictionary matrix A_l may be the same or different for different polarization measurement channels. The additive White Gaussian noise vector n_l is added into the formula. And n_l represents the measurement noise of the lth polarization channel.

3.3. Polarization GPR Imaging Based on the SMV Model. By the polarization GPR imaging method based on the SMV model, the measurement data of a single polarization channel were processed, respectively, so as to reconstruct the reflectivity of the corresponding detection scene of each polarization channel [18]. The scene reflectance vector δ_l corresponding to the lth polarization measurement channel can be reconstructed by l_1 norm minimization method, as shown in the following formula:

$$\begin{aligned} \widehat{\delta}_l &= \arg\min \left\| \delta_l \right\|_1 \\ s.t. &\left\| y_l - A_l \delta_l \right\|_2 < \varepsilon. \end{aligned} \tag{5}$$

In the formula, $||*||_1$ and $||*||_2$ represent the l_1 and l_2 norm, respectively. ε is a regularization parameter. The reconstructed δ_l is expanded according to the N_y column and the N_z row to obtain the reconstructed target image. The imaging reconstruction process represented by formula (5) only utilizes the measured data of a single polarization channel, without considering the correlation of the measured data of each polarization channel, so the imaging reconstruction effect achieved is very limited.

3.4. Polarization GPR Imaging Based on the MMV Model. In the detection process of GPR, for different polarization measurement channels, the detection area and the working frequency band of the system are the same, but the difference is only the reflectivity of the detection scene [19]. Therefore, for XX, XY, YX, and YY polarization channels, δ_l has a common sparse support set, namely, the positions of the non-zero elements of δ_l remain unchanged in the measurement, while the positions of the non-zero elements of δ_l correspond to different element values [20]. The polarization GPR imaging model based on MMV can be constructed, and the measurement data of multiple polarization channels can be processed jointly by using the multi-task Bayesian compressive sensing ($MT - BCS$) framework, so as to realize the joint reconstruction of the reflectance of the detection scene corresponding to each polarization channel. Since ($MT - BCS$) framework is based on the real-value signal model, formula (5) is converted into the real-value signal model, as shown in the following formula:

$$\widehat{y}_l = \widehat{A_l \delta_l} + \widehat{n}_l \ , \ l = [1, 2, 3, 4]. \tag{6}$$

In the formula, $\widehat{y}_l = [\mathrm{Re}(y_l)^T, \mathrm{Im}(y_l)^T]^T$, $\widehat{\delta}_l = [\mathrm{Re}(\delta_l)^T, \mathrm{Im}(\delta_l)^T]^T$, $\widehat{n}_l = \left[\mathrm{Re}(n_l)^T t, nImq(n_l)^T\right]^T$.

The dictionary matrix is shown in the following formula:

$$\widehat{A}_l = \begin{bmatrix} \mathrm{Re}(A_l) & -\mathrm{Im}(A_l) \\ \mathrm{Im}(A_l) & \mathrm{Re}(A_l) \end{bmatrix}. \tag{7}$$

In formula (6), each process of $\widehat{\delta}_l$ reconstruction from $\widehat{y}_l$ is called the lth reconstruction task, thus realizing the multi-task signal reconstruction. Given a Gaussian prior distribution with zero mean for each element of $\widehat{n}_l$ in formula (6), the Gaussian likelihood model of the measurement vector can be expressed as follows:

$$p(\widehat{y}_l \mid \widehat{n}_l, \beta) = \left(\frac{2\pi}{\beta}\right)^{-J} \exp\left(-\frac{\beta}{2}\left\| \widehat{y}_l - \widehat{A}_l \widehat{\delta}_l \right\|^2\right). \tag{8}$$

In the formula, β is the accuracy of the Gaussian density function (reciprocal of the noise variance). For each element in $\widehat{\delta}_l$, it is assumed that the Gaussian prior distribution of zero mean is satisfied, as shown in the following formula:

$$p\left(\widehat{\delta}_l | \alpha, \beta\right) = \prod_{i=1}^{2N_x N_y} N\left(\delta_l(i) | 0, \beta^{-1} \alpha_i^{-1}\right). \tag{9}$$

The hyperparameter $\alpha = \{\alpha_i\}_{i=1}^{2N_x N_y}$ is common to all four polarization channels. Therefore, the measurement vector $\widehat{y}_l$ in each task will contribute to the estimation of the hyperparameter, so as to realize the sharing of information. It is assumed that both super-parameter α and β obey gamma distribution. According to Bayes criterion, the posterior probability density function of δ_l satisfies multivariable Student-1 distribution. Its mean value is shown as follows:

$$u_1 = \left(\left(\widehat{A}_l\right)^T \widehat{A}_l + D\right)^{-1} \left(\widehat{A}_l\right)^T \widehat{y}_l . \quad (10)$$

In the formula, $D = \mathrm{diag}[\alpha_1, \alpha_1, \ldots, \alpha_{2N_xN_y}]$. The hyperparameter α is solved by the fast correlation vector machine. When the hyperparameter α is obtained, the scene reflectance vector δ_l corresponding to each polarization channel can be obtained from the following formula:

3.5. Experimental Simulation. In order to simulate the effectiveness of the mechanical fault diagnosis method of multi-measurement vectors in the line sensor network, the induction motor experimental platform was used for experimental verification, and the model performance was evaluated by statistical indicators [21]. The experimental platform used in this experiment was the induction motor experimental platform. What experimental platform collected was the vibration signals of the sensor. Here, a direction of the vibration signal was picked as the input signal of the experiment. At the data preprocessing stage, 4096 consecutive sampling data points would be contained as a sample. 300 independent samples were collected in each working condition. Therefore, as for corresponding six different induction motor running states, the entire data set consisted of 1,800 samples. At the same time, the data set was divided into the training data and the testing data in a ratio of 2:1, namely, for each working condition, there were 200 vibration signal samples for training adversation generation network, and 100 samples for model testing. The improved model was trained with the training data set and the corresponding generated samples were obtained. In the testing process, only test data (real sample data) were used to test the trained ACGAN model. At the same time, the sample quality of the generated data were evaluated. In this case, the test data were the real sample data. In the process of training, in order to prevent the generation of over-learning, a test was set up after the end of each training round. The model was used to predict the test data that did not participate in the model training, and the results were compared with the training results. If the difference was large, it indicated the existence of over-learning. The generator generated samples from the potential variable space to explore simulated learning of the distribution of input data. During the training, the Epoch of the training cycle was set to 100.1000 pseudo samples would be generated for each induction motor running state. The performance of the model is shown in Figure 3.

In the initial stage of model training, the model errors of both generator and discriminator advanced towards Nash equilibrium, but the final classification accuracy was not improved, indicating that model updating was not carried out towards the optimal solution. After 15 Epochs, the classification accuracy of the model improved significantly. The error curves of generator and discriminator were approaching Nash equilibrium and the performance of the model tended to be stable. After 60 Epochs, the error curve gradually tended to the Nash equilibrium point and the classification accuracy of the model was stable at the highest point, at which time the model had been well trained.

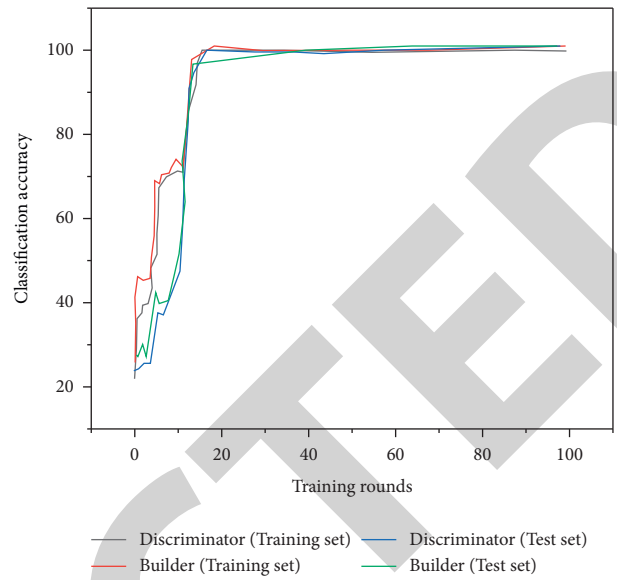

Figure 3: Diagnostic performance.

4. Result Analysis

In order to further verify the effectiveness and accuracy of the image extraction algorithm, firstly, the finite-difference time-domain (FDTD) method based on GprMax software was used to construct the detection scene and obtain the polarization GPR full-wave simulation data. Then the imaging algorithm was used to process the simulation data to obtain the imaging results. The simulation model was set as follows: The detection scene was composed of two layers of media. The first layer was air; the second layer was soil; the relative dielectric constant and conductivity of soil were $\varepsilon r = 6$ and $\delta = 1$ mS/m, respectively. Four steel bars with a radius of 0.01 m were buried in the soil, evenly arranged along the horizontal direction. The buried depth of steel bars was 0.2 m. The excitation source was a Laker wave with a center frequency of 1000 MHz and the height of the antenna from the ground was 5 cm. The transmitting antenna and the receiving antenna were in the same position and moved evenly along the horizontal direction with a moving step of 5 cm. The number of data acquisition channels was 21 and the sampling time was 20 ns. The time-domain scattering echo at each measurement aperture was obtained by FDTD calculation. Since the image acquisition algorithm was carried out in the frequency domain, the background elimination technology was first used to remove the strong reflected echo at the interface between air and soil, and then the time-domain echo data were obtained by Fourier transform to obtain the target frequency domain backscattering signal with 21 frequency points within the working bandwidth of 500–1500 MHz. The frequency step interval was 50 MHz. Thus, each polarization channel had a total of $21 \times 21 = 441$ measurement data. Additive White Gaussian noise was added to the scattering field data in

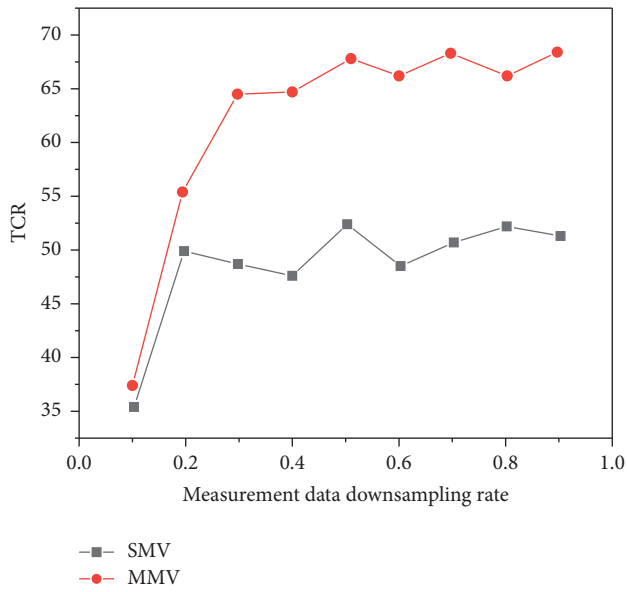

Figure 4: Imaging results at different down-sampling rates.

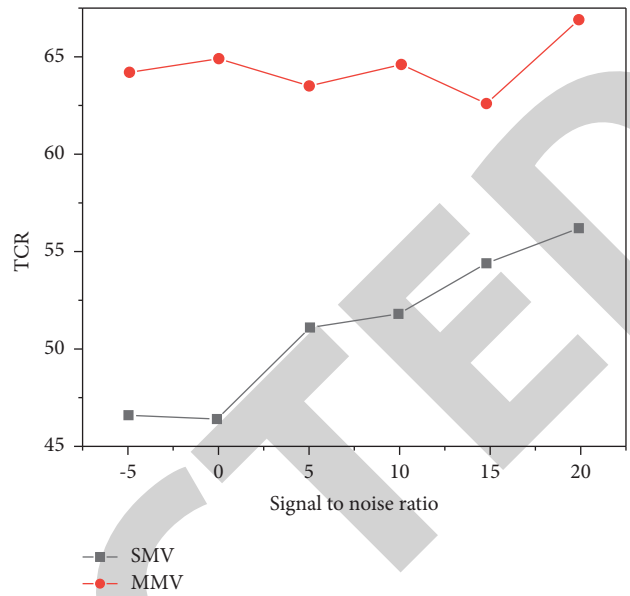

Figure 5: Imaging results at different noise ratios.

frequency domain of each polarization channel and the signal-to-noise ratio was 10 dB. The imaging area was set to 1.2 m in both horizontal direction and depth direction. The imaging region was divided into 61×61 spatial grids in the horizontal direction and depth direction [22]. In order to quantitatively compare the reconstruction performance of the two imaging algorithms under the different sampling rate reduction of measured data, the signal-to-noise ratio of the measured data was fixed at 10 dB at first, and then 100 independent experiments were conducted corresponding to the sampling rate reduction of each measured data. The average TCR of the obtained imaging results was shown in Figure 4. It could be seen from Figure 4 that under the condition of the same sampling rate reduction of measurement data, the imaging algorithm based on the MMV model had a larger TCR than the SMV model, which was more conducive to target detection and recognition.

In order to compare the imaging reconstruction performance of the two imaging algorithms under different SNRS, the reduction sampling rate of the measured data was first fixed at 0.5 and then 100 independent experiments were conducted for each SNR. The average TCR of the obtained imaging results was shown in Figure 5. It could be seen from Figure 5 that under the same SNR condition, the imaging algorithm based on the MMV model could obtain a larger TCR, and the background clutter interference energy in the imaging results was less.

At the same time, the class imbalance of training data was simulated by changing the proportion of available training data. At the same time, different numbers of generated data samples were used for experimental comparison, and the method model without data enhancement strategy was also adopted. The final classification results of fault diagnosis models under different settings were shown in Table 1. The results showed that when the training data was sufficient, the data enhancement strategy based on the adversarial generative network did not improve the classification accuracy greatly. When the proportion of available real data samples decreased to 25%, the adversarial generation network was used to generate sample data for data enhancement, so that the classification accuracy of the fault diagnosis model improved greatly. It also showed that the adversarial generative network was helpful for accurate classification of fault diagnosis models when the number of samples was limited.

Table 1: Fault diagnosis and recognition accuracy of different training datasets.

Sample number of generated data	Percentage of real data samples (%)		
	25	50 (%)	100%
0	95	91	99%
50	97	98	99%
100	98	99	99%
200	98	99	99%
300	98	100	100%

5. Conclusion

In the research, based on the sparsity of the detection scene, a polarization GPR imaging reconstruction algorithm based on the MMV model was proposed. The measurement data of multiple polarization channels were processed jointly to achieve the reconstruction of the reflectance of the detection scene corresponding to each polarization channel. The simulation data processing results based on FDTD showed that compared with the polarization GPR imaging algorithm based on the traditional SMV model, the proposed algorithm improved the accuracy of target location reconstruction and the ability of background clutter suppression significantly, which could realize the detection of buried

targets better. It also showed that the adversarial generative network was helpful for the accurate classification of fault diagnosis models when the number of samples was limited. The system could greatly improve the detection and recognition ability of underground targets. Finally, the precise positioning of the target was carried out, so as to realize the accurate judgment of mechanical failure.

Data Availability

The data used to support the findings of this study are available from the corresponding author upon request.

Conflicts of Interest

The author declares that there are no conflicts of interest.

References

[1] W. Li and D. Liu, *Parametric Variational Sum-roduct Algorithm for Cooperative Localization in Wireless Sensor Networks*, no. 99, p. 1, IEEE Access, USA, 2021.

[2] O. A. Mahdi, A. B. Ghazi, and Y. R. B. Al-MayoufAl-Mayouf, "Void-hole aware and reliable data forwarding strategy for underwater wireless sensor networks," *Journal of Intelligent Systems*, vol. 30, no. 1, pp. 564–577, 2021.

[3] J. C. Gonzalez-Arango, D. C. Ocampo-Munera, L. F. Castano-LondonoCastano-Londono, G. D. Goez-SanchezGoez-Sanchez, and R. A. Velasquez-VelezVelasquez-Velez, "Performance evaluation of symmetric cryptographic algorithms in resource constrained hardware for wireless sensor networks," *IEEE Latin America Transactions*, vol. 19, no. 10, pp. 1632–1639, 2021.

[4] S. Hriez, S. Almajali, H. Elgala, M. Ayyash, and H. B. Salameh, "A novel trust-aware and energy-aware clustering method that uses stochastic fractal search in iot-enabled wireless sensor networks," *IEEE Systems Journal*, vol. 16, no. 99, pp. 1–12, 2021.

[5] H. Shahid, H. Ashraf, H. Javed, M. Humayun, N. JhanjhiJhanjhi, and M. A AlZain, "Energy optimised security against wormhole attack in iot-based wireless sensor networks," *Computers, Materials & Continua*, vol. 68, no. 2, pp. 1967–1981, 2021.

[6] Q. Qi, Y. Li, and Q. Guo, "A convex relaxation algorithm for source localization considering sensor motion in wireless sensor networks," *IEEE Communications Letters*, vol. 25, no. 6, pp. 1867–1871, 2021.

[7] A. Sharma and R. Kumar, "A constrained framework for context-aware remote E-healthcare (CARE) services," *Transactions on Emerging Telecommunications Technologies*, vol. 33, 2019.

[8] D. H. KimKim and S. M. SchweitzKoo, "Effect of gas annealing on the electrical properties of Ni/AlN/SiC," *Micromachines*, vol. 12, no. 3, pp. 283–287, 2021.

[9] C. Gong, D. Xie, C. Guo, and S. Kherbachi, "Transmission control under multi-service disciplines in wireless sensor networks," *Computers, Materials & Continua*, vol. 68, no. 2, pp. 2127–2143, 2021.

[10] S. Shriram, B. NagarajNagaraj, J. JayaJaya, S. ShankarShankar, and P. Ajay, "Deep learning-based real-time AI virtual mouse system using computer vision to avoid COVID-19 spread," *Journal of Healthcare Engineering*, vol. 2021, Article ID 8133076, 8 pages, 2021.

[11] B. Ma, W. Cai, Y. Han, and G. Yu, "A novel probability confidence CNN model and its application in mechanical fault diagnosis," *IEEE Transactions on Instrumentation and Measurement*, vol. 70, no. 99, pp. 1–11, 2021.

[12] A. Bashar and S. S, "Physical layer protection against sensor eavesdropper channels in wireless sensor networks," *June 2021*, vol. 3, no. 2, pp. 59–67, 2021.

[13] N. Ping, P. Sun, and Q. Kang, "Retraction note to: correlation of air pollutants and prediction of physical fitness index based on wireless sensor network," *Arabian Journal of Geosciences*, vol. 14, no. 22, pp. 2394–2401, 2021.

[14] J. Chen, J. Liu, X. Liu, X. Xu, and F. Zhong, "Decomposition of toluene with a combined plasma photolysis (CPP) reactor: influence of UV irradiation and byproduct analysis," *Plasma Chemistry and Plasma Processing*, vol. 41, no. 1, pp. 409–420, 2020.

[15] K. Koosheshi, "Two novel protocols for optimizing energy consumption in heterogeneous wireless sensor networks using fuzzy logic for monitoring, diagnosis and target tracking," *SN Applied Sciences*, vol. 3, no. 4, pp. 512–520, 2021.

[16] R. Huang, S. Zhang, W. Zhang, and X. Yang, "Progress of zinc oxide-based nanocomposites in the textile industry," *IET Collaborative Intelligent Manufacturing*, vol. 3, no. 3, pp. 281–289, 2021.

[17] H. Malik and A. Almutairic, *Modified Fuzzy-Q-Learning (MFQL)-based Mechanical Fault Diagnosis for Direct-Drive Wind Turbines Using Electrical Signals*, no. 99, p. 1, IEEE Access, USA, 2021.

[18] R. Kumar, J. Gill, and B. P. Dahiya, "Hybrid optimization in wireless sensor networks to improve network lifetime," *Türk Fizyoterapi ve Rehabilitasyon Dergisi/Turkish Journal of Physiotherapy and Rehabilitation*, vol. 32, no. 2, pp. 3571–3582, 2021.

[19] M. Srinivas and T. Amgoth, "Data acquisition in large-scale wireless sensor networks using multiple mobile sinks: a hierarchical clustering approach," *Wireless Networks*, vol. 28, no. 2, pp. 603–619, 2022.

[20] Q. Liu, W. Zhang, M. W. BhattBhatt, and A. Kumar, "Seismic nonlinear vibration control algorithm for high-rise buildings," *Nonlinear Engineering*, vol. 10, no. 1, pp. 574–582, 2021.

[21] L. Cao, Y. Yue, Y. Cai, and Y. Zhang, "A novel coverage optimization strategy for heterogeneous wireless sensor networks based on connectivity and reliability," *IEEE Access*, vol. 9, no. 99, pp. 18424–18442, 2021.

[22] R. A. Nazib and S. Moh, *Energyfficient and Fast Data Collection in UAV-ided Wireless Sensor Networks for Hilly Terrains*, no. 99, p. 1, IEEE Access, USA, 2021.